Applied Physics A (2023) 129:876
https://doi.org/10.1007/s00339-023-07164-1

Applied Physics A
Materials Science & Processing

Chemically synthesized facet-controlled visible light active $BiVO_4$ thin films for photoelectrochemical water splitting

Shirin P. Kulkarni[1] · Yogesh M. Chitare[1] · Vikas V. Magdum[1] · Prashant D. Sawant[1] · Shweta V. Talekar[1] · Shraddha A. Pawar[1] · Umakant M. Patil[1] · Kishor V. Gurav[2] · Dhanaji B. Malavekar[3] · Amol U. Pawar[4] · Jayavant L. Gunjakar[1]

Received: 4 September 2023 / Accepted: 14 November 2023 / Published online: 1 December 2023

Abstract
The facile and cost-effective chemical bath deposition (CBD) method is used to synthesize highly photoactive facet-controlled bismuth vanadate ($BiVO_4$) thin films on glass and stainless steel (SS) substrates. The facet-controlled $BiVO_4$ thin films are synthesized by variation in anionic precursor with fine tuning of chemical bath pH from alkaline to acidic media. The variation of anionic precursor evolves the morphology of $BiVO_4$ from dispersed nanoparticles to faceted microcrystals. Furthermore, the fine-tuning of chemical bath pH leads to the well-defined octahedral $BiVO_4$ microcrystals. Compared to dispersed nanoparticulate $BiVO_4$ photoanodes, the octahedral $BiVO_4$ photoanodes demonstrated superior photocurrent density of 2.75 mA cm^{-2} (at 1.23 V vs. RHE), good photostability and charge separation efficiency (45.5%) owing to their excellent PEC reaction kinetics. The present study underscores the usefulness of the CBD method for facet-controlled synthesis of semiconducting thin films for different photo-functional applications.

Keywords $BiVO_4$ · CBD · Microstructure · Photoanode · Photoelectrochemical performance · Water splitting

1 Introduction

In recent years, energy crises and environmental pollution have increased market demands for clean energy storage sources that can replace fossil fuels and provide energy when needed. Sustainable hydrogen (H_2) production is a key challenge for developing alternative energy systems that provide an environmentally friendly and inexpensive energy supply [1, 2]. Among the numerous renewable energy sources, solar energy has tremendous potential for energy conversion as it is one of the most abundant, cost-free and clean sources [3]. The conversion of solar energy into H_2 via the solar-assisted water-splitting process is one of the most promising technologies because of its potential for green and sustainable H_2 production [4]. Photoelectrochemical (PEC) water-splitting technology has emerged as an effective approach for producing H_2 using semiconducting photoelectrodes [5]. The PEC water-splitting is an environmentally friendly process, because it uses natural sunlight for water-splitting reactions in the presence of semiconductor photoelectrode.

During the past few decades, ZnO and TiO_2 have been extensively studied as photoelectrodes in PEC water splitting due to their high chemical stability and non-toxicity [6, 7]. However, their performance is limited owing to the wide bandgap energy (absorb only ultraviolet radiations; < 4% of solar spectrum). Hence, lots of efforts were put forward on narrow bandgap materials, such as doped-metal oxides, metal sulfides and nitrides for improved PEC water splitting [8–12]. Compared with other photocatalysts, $BiVO_4$ with suitable bandgap energy (~ 2.4 eV), highest photostability, high optical absorption coefficient, least photo-corrosion,

✉ Jayavant L. Gunjakar
jlgunjakar@gmail.com

[1] Centre for Interdisciplinary Research, D. Y. Patil Education Society (Deemed to Be University), Kolhapur, MS 416 006, India

[2] Energy Conversion and Storage Research Laboratory, Department of Physics, Devchand College, Arjunnagar, MS 591 237, India

[3] Department of Materials Science and Engineering, Optoelectronic Convergence Research Centre, Chonnam National University, Gwangju 61186, South Korea

[4] Environmental and Climate Technology, Korea Institute of Energy Technology, Naju-Si, Jeollanamdo 58219, Republic of Korea

low toxicity, high theoretical solar-to-hydrogen conversion efficiency and appropriate band structure for water splitting reaction can be the best choice as a photoelectrode for PEC water splitting application [13, 14].

Considering that the photoactivity of semiconductors is highly dependent on their surface structure, the faceted growth of $BiVO_4$ is highly desirable. Such growth can assist the migration of photogenerated electrons and holes to the particular crystal facets, leading to better charge separation and improved quantum efficiency for PEC water splitting [15–17]. From this insight, several reports are available on the faceted growth of $BiVO_4$ by various high-temperature chemical methods, such as hydrothermal, urea hydrolysis and solvothermal [18–25]. Compared to other chemical methods, chemical bath deposition (CBD) is an inexpensive, simple and convenient method for large-area coating carried out in air at room temperature with various substrates. It facilitates better orientation of crystallites with improved grain structure with pinhole-free and uniform deposits. Stoichiometry of deposits is highly maintained as basic building blocks are ions instead of atoms. There are no organo-metallic solvents and no toxic or pyrolyzed gases evolved [26]. Hence, intense research interest has been focused on the faceted growth of $BiVO_4$ by CBD method.

In one instance, the chemically deposited $BiVO_4$ thin films displayed faceted growth of $BiVO_4$ with micrometric and square prism particle morphology [27]. Similarly, the $BiVO_4$ photoanodes with exposed (040) facets were fabricated by the modified CBD method in a neutral bath [28]. Moreover, the CBD method reported the decahedron-shaped duel-faceted $BiVO_4$ microcrystals coated on FTO substrates [29]. Though these all are faceted microstructures, their PEC performance is poor. Compared to other faceted microstructures, an octahedral shape with {121} exposed facets is more effective for photo-functional activity [30].

Even though there is one report on the deposition of octahedral $BiVO_4$ microcrystals by CBD; a detailed study on the morphology evolution of $BiVO_4$ from nanoparticulate to faceted by precursor variation is not reported yet [31]. In the present work, facet-controlled $BiVO_4$ thin film photoanodes are synthesized by variation in anionic precursor with fine tuning of chemical bath pH from alkaline to neutral to acidic media without buffer solution. The evolution of physicochemical and visible-light-induced PEC properties of $BiVO_4$ are investigated to probe the effect of change in bath composition.

2 Experimental section

2.1 Materials

Bismuth nitrate pentahydrate ($Bi(NO_3)_3{\cdot}5H_2O$), sodium orthovanadate (Na_3VO_4), sodium metavanadate ($NaVO_3$), ethylene diamine tetra acetic acid (EDTA) disodium salt ($C_{10}H_{14}N_2Na_2O_8$) and sodium hydroxide (NaOH) were purchased from Sigma-Aldrich and used without further purifications. Stainless steel (SS) substrates and glass slides were used to deposit $BiVO_4$ thin films.

2.2 Synthesis of $BiVO_4$ thin films

The glass substrates were cleaned in an ultrasonic bath using labolene detergent, double distilled water (DDW), acetone, ethanol, and again in DDW. The SS substrates were first cleaned with zero-grade polish paper, followed by washing in acetone, ethanol, and again in DDW. Thoroughly cleaned glass and SS substrates were stored in deionized water before use.

$BiVO_4$ thin films were deposited on well-cleaned glass and SS substrates by the CBD method with a change in anionic precursor and deposition bath pH. A chemical bath for the deposition of $BiVO_4$ thin films was prepared from an aqueous solution of bismuth precursor ($Bi(NO_3)_3{\cdot}5H_2O$; 25 mM) complexed with EDTA disodium salt (25 mM) under constant stirring. As another precursor, the aqueous solution of vanadium (Na_3VO_4 or $NaVO_3$; 25 mM) was prepared. The chemical deposition bath was obtained by dropwise addition of vanadium precursor solution into the bismuth complex under constant stirring. The final pH of the bath was adjusted to alkaline (8.5), neutral (7) and acidic (5.5) with the addition of an aqueous 1 M NaOH solution. After pH maintenance, the bath was heated at 85℃ under constant stirring for 1 h to obtain a transparent pale yellow color solution. Furthermore, the obtained solution was cooled down to room temperature and used as a deposition solution.

The above deposition bath composed of $Bi(NO_3)_3{\cdot}5H_2O$ and Na_3VO_4 precursors was named as bath A, and that with $Bi(NO_3)_3{\cdot}5H_2O$ and $NaVO_3$ precursors was denoted as bath B. The well-cleaned glass and SS substrates were placed in the deposition bath. During the deposition process, the deposition vessel was closed and kept in a water bath at 85 ℃ for 10 h. After the deposition, $BiVO_4$-coated substrates were removed from the bath, washed with DDW and air dried. Afterward, the as-prepared yellowish orange colored $BiVO_4$ thin films were annealed at 400 ℃ for 2 h to get well-crystalline $BiVO_4$ thin films. The schematic representation of the $BiVO_4$ thin film deposition process is shown in Fig. 1. The annealed $BiVO_4$ samples prepared from bath A at pH 5.5, 7 and 8.5 are represented as O_{Acd}, O_{Nut} and O_{Alk}, respectively. Similarly, the annealed $BiVO_4$ samples prepared from bath B at pH 5.5, 7 and 8.5 are represented as M_{Acd}, M_{Nut} and M_{Alk}, respectively.

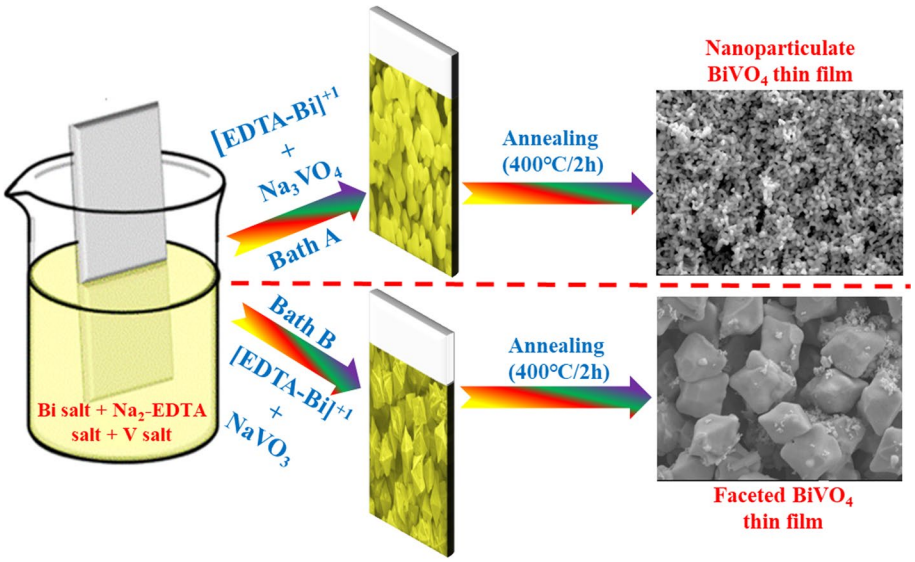

Fig. 1 Schematic representation of the deposition of $BiVO_4$ thin films by CBD method

2.3 Materials characterizations

The X-ray diffraction (XRD) analysis was used to study the crystal structure and orientation of deposited thin films with the help of Rigaku miniflex 600 Diffractometer (Cu k_α radiation: $\lambda = 1.5406$ Å). The micro-Raman spectra were collected using a FLEX G spectrometer (Tokyo Instrument, Japan) having an excitation wavelength of 532 nm. The Fourier transform infrared (FT-IR) spectroscopy analysis was used to examine the chemical bonding of $BiVO_4$ (αT Bruker). The oxidation states of elements present on the surface of $BiVO_4$ were investigated with X-ray photoelectron spectroscopy (Thermo VG Scientific Multitab 2000 XPS with Al K_α (1486.6 eV) X-ray source). The morphological features and chemical composition of elements present in the $BiVO_4$ thin films were estimated with scanning electron microscopy (SEM) JEOL JSM-7900 F equipped with energy-dispersive spectroscopy (EDS)-elemental mapping analysis. The ultraviolet–visible diffuse reflectance spectroscopy (UV–Vis DRS) was used to probe the optical properties of $BiVO_4$ thin films using a Jasco spectrometer.

2.4 Electrochemical and photoelectrochemical measurements

The band structure of $BiVO_4$ was estimated from the cyclic voltammetry (CV) measurements performed in sodium perchlorate ($NaClO_4$) electrolyte using CHI650D electrochemical workstation. In three electrode configuration, $BiVO_4$ thin film deposited on SS substrate, platinum plate and Ag/AgCl were utilized as working, counter and reference electrodes, respectively.

The PEC characteristics of $BiVO_4$ photoanodes were studied with linear sweep voltammetry (LSV) and chronoamperometry measurements. All the PEC measurements were carried out with CHI650D electrochemical workstation and standard three-electrode configuration. The three-electrode assembly was composed of $BiVO_4$ thin film deposited on SS substrate, saturated calomel electrode (SCE) and platinum plate as working, reference and counter electrode, respectively. 0.1 M potassium phosphate buffer solution (pH 7) was used as an electrolyte. In addition, during the PEC measurements, 0.2 M sodium sulfite (Na_2SO_3) was added to the electrolyte solution, which served as a hole scavenger that minimized the rate of recombination of charge carriers and hence increased the PEC performance [32].

The photocurrent of $BiVO_4$ photoanodes was measured under front illumination with a light intensity of 100 mW cm^{-2} simulated by the AM 1.5 G and 420 nm optical cutoff filters from 35 W xenon lamp. During the PEC experiments, photocurrent was measured by either applying a fixed potential or sweeping the potential to the positive direction with a scan rate of 10 mV s^{-1}. Samples were tested in the chopped illumination arrangement to measure the transient photocurrents. All the electrochemical results were stated against the reversible hydrogen electrode (RHE) scale. Following equations represents the interconversion between potentials vs. RHE and vs. SCE scales [33]:

$$E(\text{vsRHE}) = E(\text{vsSCE}) + E\text{SCE(reference)} + 0.0591V \times \text{pH},$$

$$V(\text{vsRHE}) = V(\text{vs.SCE}) + 0.654\text{V}.$$

Applied Bias Photon to Current Efficiency (ABPE):

The applied bias photon to current efficiency (ABPE) was estimated from photocurrent density vs. potential

(J–V) measurements assuming 100% Faradaic efficiency with the help of the following formula:

$$\mathrm{ABPE}(\%) = \left[\frac{J\left(\mathrm{mAcm^{-2}}\right) \times \left(1.23 - V_{\mathrm{bias}}\right) \times (V)}{P_{\mathrm{in}}(\mathrm{mWcm^{-2}})}\right]_{\mathrm{AM1.5G}} \times 100,$$

where J represents the photocurrent density, V_{bias} is the applied potential and P_{in} is the incident illumination power density at 1 Sun illumination (AM 1.5 G, 100 mW $\mathrm{cm^{-2}}$).

Furthermore, the charge separation efficiency (η_{bulk}) of $BiVO_4$ photoanodes was estimated using the following equation [34]:

$$\eta_{\mathrm{bulk}} = \frac{J\mathrm{Na_2So_3}}{J\mathrm{abs}},$$

where $J_{\mathrm{Na_2SO_3}}$ and J_{abs} (7.5 mA $\mathrm{cm^{-2}}$) represents the measured photocurrent density in the presence of a hole scavenger and the theoretical photocurrent density of $BiVO_4$, respectively.

3 Results and discussion

3.1 Reaction mechanism for the deposition of $BiVO_4$

Deposition of the thin film via the CBD method is based on the principle of controlled precipitation of desired material over the heterogeneous substrate surface. During the deposition of $BiVO_4$ thin films, the aqueous supersaturated solution of $[EDTA–Bi]^{+1}$ complex and Na_3VO_4 or $NaVO_3$ transforms into a saturated state via precipitation of $BiVO_4$.

Initially, the reaction of $Bi(NO_3)_3$ with EDTA disodium salt gives $[EDTA–Bi]^{+1}$ complex (represented in the following reaction), which avoids the spontaneous precipitation in the bath [31]:

$$[\mathrm{EDTA}]^{2-} + \mathrm{Bi}^{3+} \rightarrow [\mathrm{EDTA} - \mathrm{Bi}]^{+1}.$$

On the other hand, the aqueous solution of vanadium (Na_3VO_4 or $NaVO_3$) was prepared as another precursor. The hydrolysis reaction of vanadium leading various polyoxovanadate (POV) anions, such as layered oxides $[V_2O_5]$, chain metavanadates $[VO_3^-]_n$ and compact polyanions $[V_{10}O_{28}]^{6-}$ as represented in the following reaction [35, 36]:

$$\left[V(\mathrm{OH_2})_6\right]^{5+} + h\mathrm{H_2O} \rightarrow [V(\mathrm{OH})_h\left(\mathrm{OH_2}\right)_{6-h}]^{(5-h)+} + h\mathrm{H_3O^+}.$$

The structure of POV anions is concentration and pH dependent [36, 37]. In the above reaction, the hydrolysis ratio (h) increases with the pH, forming aquo, hydroxo, or oxo vanadium species [35, 36]. In previous reports, the structure and stability of POV anions are reported [36, 37].

The chemical deposition bath for $BiVO_4$ was obtained by adding vanadium precursor solution (Na_3VO_4 or $NaVO_3$) into a $[EDTA–Bi]^{+1}$ complex solution. As a result, the milky white color of the bismuth solution was changed to a yellowish-orange color and the solution became supersaturated. The final pH of the chemical bath was adjusted to alkaline (8.5), neutral (7) and acidic (5.5) with the addition of aqueous 1 M NaOH solution. At pH 5.5, $[V_{10}O_{27}(OH)]^{5-}$ prominent vanadium species are present in the chemical bath, while $[V_3O_9]^{3-}$ species are present at pH 7 and 8.5 [36].

Afterward, the chemical bath was kept at an elevated temperature of 85 ℃ with vertically immersed substrates. During this process, continuous deprotonation occurred that led to the transformation of POV anions to oxovanadium anions VO_4^{3-} [37]. Simultaneously, $[EDTA–Bi]^{+1}$ complex dissociated by releasing free Bi^{3+} cations, which then react with VO_4^{3-} anions present in the chemical bath [31]. Consequently, the solution became saturated, leading to precipitation through the heterogeneous (on the substrate surface) and homogeneous growth of the $BiVO_4$, as represented by the following reaction.

The above reaction is susceptible to the release rate of free Bi^{+3} cations and deprotonation of POV anions that led to various $BiVO_4$ growth rates from baths A and B. These growth rate variations can cause the microstructural evolution of $BiVO_4$. Typically, 'bath A' composed of Na_3VO_4 and $[EDTA–Bi]^{+1}$ complex, release faster free Bi^{+3} cations and deprotonated VO_4^{3-} anions, due to easily available VO_4^{3-} anions ($Na_3VO_4 \rightarrow 3Na^+ + VO_4^{3-}$), which leads to the rapid formation of $BiVO_4$ [36]. In this process, the nucleation centers and activation sites were maximum; consequently, $BiVO_4$ particle size became smaller and nanoparticulate $BiVO_4$ formed. Conversely, 'bath B' composed of $[EDTA–Bi]^{+1}$ complex and $NaVO_3$, released slow Bi^{+3} cations and deprotonated VO_4^{3-} anions, which led to the slow growth of $BiVO_4$. The slow growth of $BiVO_4$ can be attributed to the absence of VO_4^{3-} anions in the initial state. As a result, it requires time for the formation of VO_4^{3-} anions through the following reactions: $NaVO_3 + 2NaOH \rightarrow Na_3VO_4 + H_2O$ and $Na_3VO_4 \rightarrow 3Na^+ + VO_4^{3-}$. This ultimately hinders the growth of $BiVO_4$ [38]. In this process, nucleation centers and activation sites were low, resulting in faceted octahedral growth of $BiVO_4$. Moreover, maintaining the acidic pH of 'bath B' further slowed the release of Bi^{+3} cations and deprotonated VO_4^{3-} anions, which led to the slow growth of $BiVO_4$. Thus, well-defined octahedral-shaped $BiVO_4$ microcrystal morphology was evolved for the acidic pH of 'bath B'. Thus, by adjusting the chemical bath composition, one can effectively tune the $BiVO_4$ crystal morphology from nanoparticulate to faceted octahedral morphologies.

3.2 Characterizations of $BiVO_4$

3.2.1 Structural analysis

The crystallographic properties of deposited $BiVO_4$ thin films were probed with the XRD technique, as shown in Fig. 2. All $BiVO_4$ thin films display typical Braggs reflections that match the monoclinic (I2/a) $BiVO_4$ phase (JCPDS no.: 14-0688). Interestingly apparent peak splitting is observed at 19°, 35° and 46° indicating the formation of a monoclinic scheelite $BiVO_4$ phase [39]. In the monoclinic scheelite $BiVO_4$ phase, each bismuth and vanadium ion are co-ordinally bonded to eight and four oxygen atoms, respectively [40]. As represented in Fig. 2c, each bismuth ion is bound to eight VO_4 tetrahedral units (Crystallography Open Database card no. 9013437). The estimated lattice parameters $a = 5.27$ Å, $b = 11.60$ Å and $c = 5.087$ Å of $BiVO_4$ are in good agreement with the monoclinic scheelite $BiVO_4$ phase.

Moreover, all the $BiVO_4$ thin films deposited from baths A and B display significant variation in the relative intensities of the XRD peaks. This variation in the relative intensities of the XRD peaks with the highest intensity (121) plane indicates the preferential growth of the $BiVO_4$ crystals. The intensity ratio of (121)/(040) characteristic XRD peaks is calculated and denoted as R, which varies with the synthesis conditions of $BiVO_4$ thin films. The intensity ratio R for the $BiVO_4$ thin films deposited from bath A is 1.63, 1.57 and 3.25 for O_{Acd}, O_{Nut} and O_{Alk} samples, respectively. Similarly, R for the $BiVO_4$ thin films deposited from baths B is 6.44, 9.75 and 3.52 for M_{Acd}, M_{Nut} and M_{Alk} samples, respectively. This change in R is characteristic of the preferential growth of the $BiVO_4$ crystals. According to variation in R, the $BiVO_4$ thin films deposited from baths A and B display the dispersed nanoparticle and preferentially grown faceted octahedral surface morphology, respectively. According to Scherrer's formula, the mean crystallite sizes estimated for $BiVO_4$ crystals deposited from baths A and B are 10 nm and 511 nm, respectively.

3.2.2 Chemical bonding analysis

The chemical bonding characteristics of the $BiVO_4$ thin films deposited from baths A and B were probed with Raman spectroscopy, as shown in Fig. 3. The Raman peaks P_1 (131 cm^{-1}) and P_2 (212 cm^{-1}) at lower frequency regions are assigned to the external rotation or translation modes of $BiVO_4$ [41]. All the $BiVO_4$ samples display typical Raman bands P_3 (325 cm^{-1}) and P_4 (367 cm^{-1}), corresponding to the asymmetric (Bg symmetry) and symmetric (Ag symmetry) bending modes of the VO_4 tetrahedron, respectively [42]. The peaks P_5 (710 cm^{-1}) and P_6 (826 cm^{-1}) are assigned to the asymmetric (V–O) stretching mode and symmetric (V–O) stretching modes, respectively [41–43]. The present Raman features confirm the pure monoclinic scheelite $BiVO_4$ phase deposition from both baths. Furthermore, the functional groups

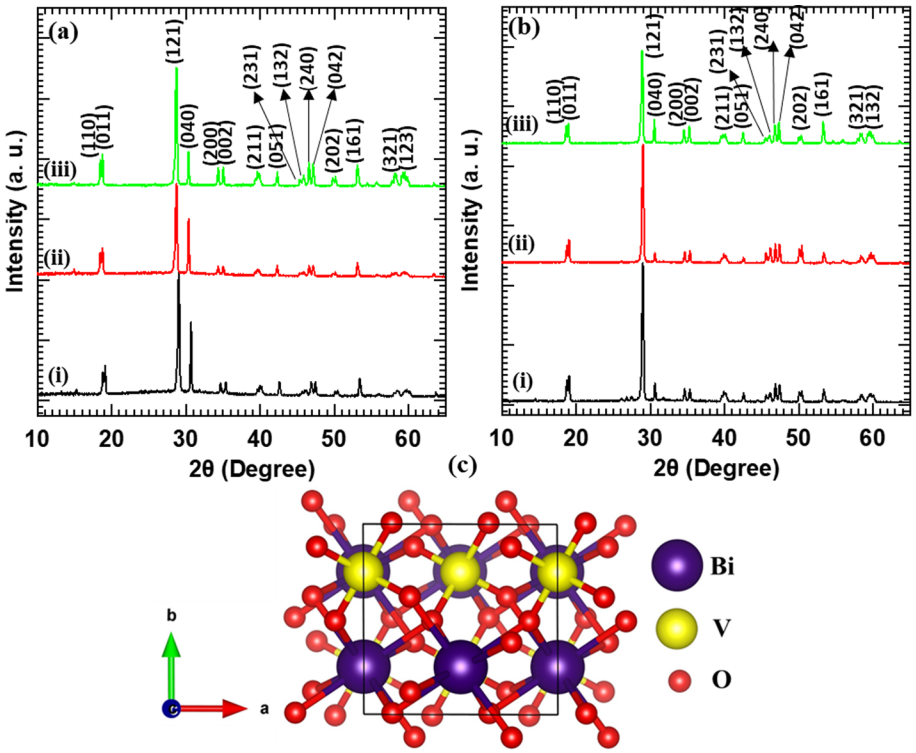

Fig. 2 XRD patterns of $BiVO_4$ thin films deposited from **a** bath A [O_{Acd} (i), O_{Nut} (ii), O_{Alk} (iii)] and **b** bath B [M_{Acd} (i), M_{Nut} (ii), M_{Alk} (iii)]. **c** $BiVO_4$ crystal structure drawn from Vesta software

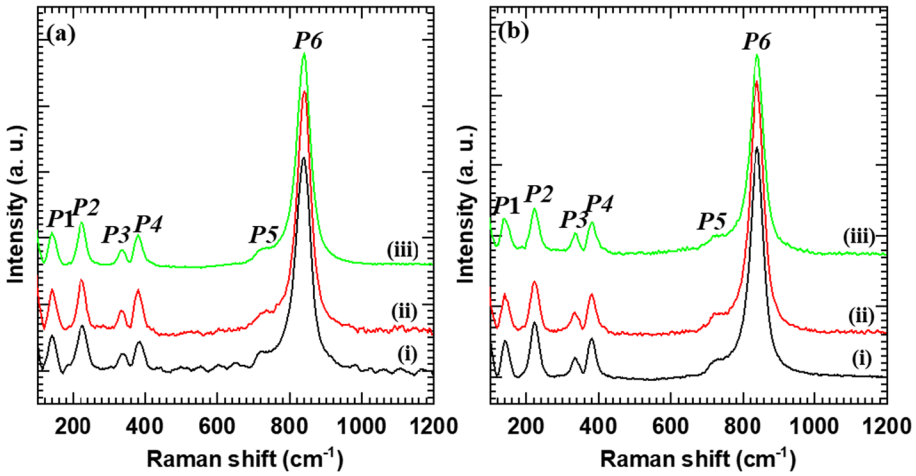

Fig. 3 Micro-Raman spectra of $BiVO_4$ thin films deposited from **a** bath A [O_{Acd} (i), O_{Nut} (ii), O_{Alk} (iii)] and **b** bath B [M_{Acd} (i), M_{Nut} (ii), M_{Alk} (iii)]

present on the $BiVO_4$ thin film surface were analyzed with FTIR spectroscopy, as shown in Fig. S2 (ESI). The $BiVO_4$ thin films deposited from both baths display distinct IR bands corresponding to the monoclinic scheelite $BiVO_4$ phase, indicating no organic impurities attached to the surface of deposited $BiVO_4$ crystals.

3.2.3 XPS analysis

The XPS technique was used to probe the chemical constituents and oxidation states of elements in $BiVO_4$ thin films. The survey XPS spectra commonly show the spectral features for the Bi, V and O elements in $BiVO_4$ thin films

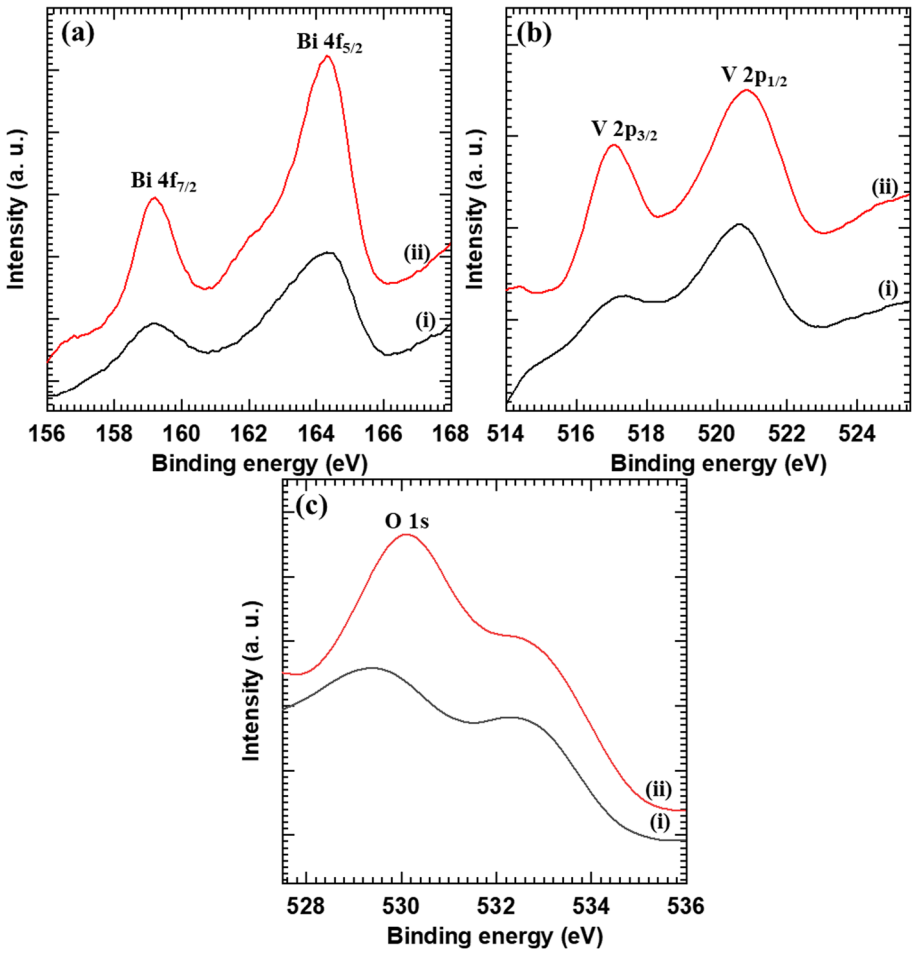

Fig. 4 **a** Bi 4f, **b** V 2p, **c** O 1 s XPS spectra of (i) $BiVO_4$ deposited from bath A (O_{Acd}) and (ii) $BiVO_4$ deposited from bath B (M_{Acd})

(Fig. S3 ESI). Figure 4 represents the Bi 4f, V 2p and O 1 s core level XPS spectra of $BiVO_4$ thin films deposited from baths A and B. Figure 4a shows the high-resolution Bi 4f XPS spectra of the $BiVO_4$ thin films. Both $BiVO_4$ thin films deposited from baths A and B show intense peak doublet at 164.2 eV and 158.9 eV assigned to the Bi $4f_{5/2}$ and Bi $4f_{7/2}$, respectively, confirming the Bi^{+3} state [44]. The V 2p XPS spectra of $BiVO_4$ thin films in Fig. 4b show two broad peaks at binding energies (BEs) of 516.4 and 520.8 eV corresponding to the spin–orbit splitting of V $2p_{3/2}$ and V $2p_{1/2}$, respectively [45]. These spectral features are characteristic of pentavalent V in $BiVO_4$ thin films. As shown in Fig. 4c, the high-resolution O 1 s XPS spectra of $BiVO_4$ thin films exhibit a broad peak at 529.5 eV with a shoulder at 533.1 eV. The broad peak at 529.5 eV is assigned to the oxygen from the $BiVO_4$ lattice, and the shoulder is attributed to the OH^- groups (originating from structural or adsorbed water molecules and oxygen vacancies) on the surface of the sample [44]. The present XPS results clearly show the trivalent and pentavalent states of Bi and V in $BiVO_4$, respectively, which confirms the formation of pure phase $BiVO_4$ from both baths.

3.2.4 Morphological and compositional analysis

SEM analysis was used to investigate the surface morphology of $BiVO_4$ thin films. The anionic precursor variation significantly affected the $BiVO_4$ morphology, as shown in Fig. 5. The $BiVO_4$ thin films deposited from bath A (O_{Alk}) show dispersed particle morphology with an average size of 0.45 µm. In addition, O_{Nut} and O_{Acd} samples have similar nanoparticulate morphology as that of O_{Alk}, as shown in Fig. S4 (ESI). On the other hand, that deposited from bath B (M_{Alk}) shows faceted microcrystal morphology with an average size of 5 µm. The present SEM analysis provides strong evidence for the change in morphology from the dispersed particles to facet-controlled $BiVO_4$ thin films by changing the anionic precursor.

Furthermore, the chemical composition of the $BiVO_4$ thin films deposited from baths A and B was probed with EDS analysis, as shown in Figs. S5–S6 (ESI) and Fig. 6. The $BiVO_4$ thin films deposited from baths A and B display uniform distribution of constituent elements [bismuth (Bi), vanadium (V) and oxygen (O)] in the nanometer scale mapping region with a Bi/V ratio of 1. Present results indicate the uniform growth of $BiVO_4$ from both baths without any special phase separation.

As shown in Figs. 5 and 7, all the $BiVO_4$ thin films deposited from bath B display shape-selective octahedral crystals, which agrees with the XRD results showing an intense (121) peak and quenched (040) XRD peaks in these films. The pH of bath B significantly affects the crystal shape and size. The shape of the $BiVO_4$ crystals changes from faceted microcrystals to well-defined octahedra as the pH changes from alkaline to acidic media. The M_{Alk} thin film show coarse octahedral-shaped microcrystals with significantly truncated vertices and blunt edges. On the other hand, the M_{Acd} thin film show well-defined octahedral-shaped microcrystals with mildly truncated vertices and sharp edges. M_{Nut} sample has a similar type of octahedral

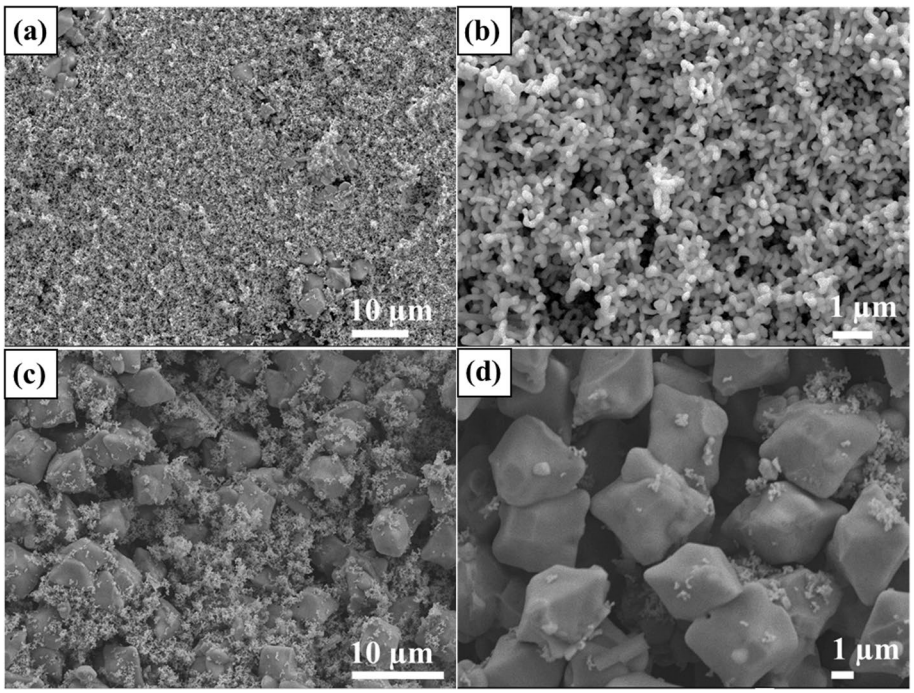

Fig. 5 SEM images of **a**, **b** $BiVO_4$ thin films deposited from bath A (O_{Alk}) and **c**, **d** bath B (M_{Alk})

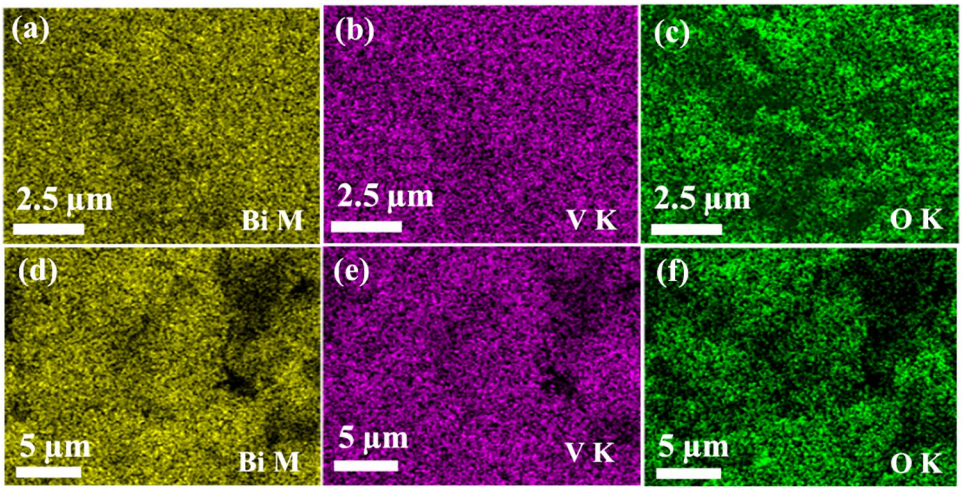

Fig. 6 EDS elemental mapping of **a**–**c** $BiVO_4$ deposited from bath A (O_{Acd}) and **d**–**f** $BiVO_4$ deposited from bath B (M_{Acd})

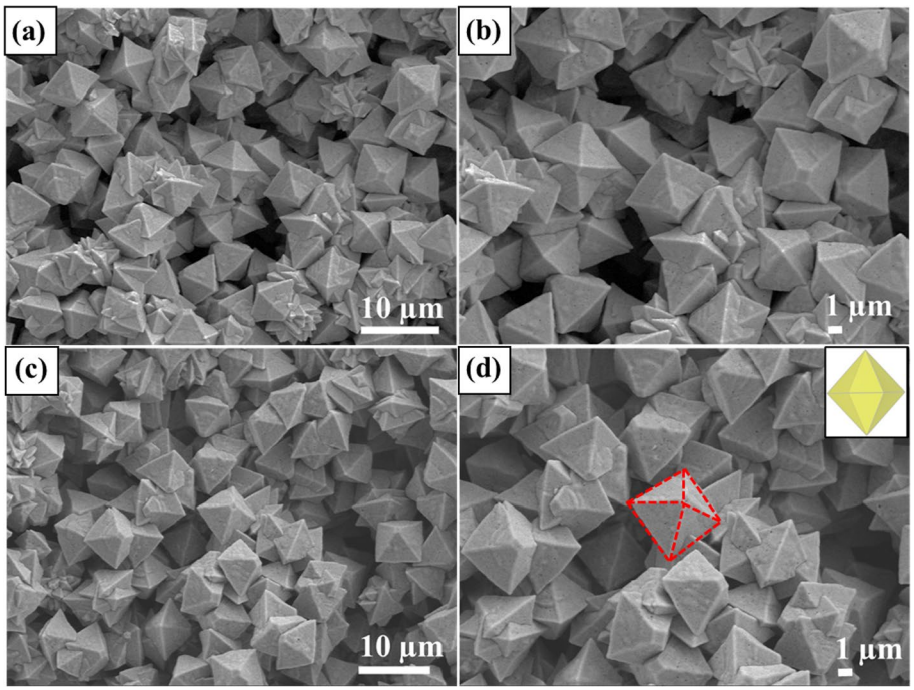

Fig. 7 SEM images of **a**, **b** M_{Nut} and **c**, **d** M_{Acd} $BiVO_4$ thin films

morphology as compared to M_{Acd} sample. In addition, from the XRD data, the *R* values of M_{Nut} and M_{Acd} are 9.75 and 6.44, respectively. Though the M_{Acd} sample displays slightly less *R* value, it showed compact and sharp $BiVO_4$ microcrystallites. In addition, the size of octahedral microcrystals deposited at acidic pH of 5.5 is reduced compared to that synthesized at alkaline pH. The present result underscores the importance of pH variation for the shape-selective synthesis of $BiVO_4$. Among the three samples, $BiVO_4$ deposited from an acidic bath shows the well-defined facet-controlled octahedral morphology, which can be advantageous for visible light-induced PEC measurements.

3.2.5 Optical analysis

The band structure and optical properties of the $BiVO_4$ thin films are studied with diffuse reflectance UV–Vis spectroscopy. As shown in Fig. 8, the dispersed nanoparticles and faceted $BiVO_4$ thin films display significant absorption in the visible light region, indicating the visible-light harvesting ability of $BiVO_4$ thin films. The electronic structure of monoclinic scheelite $BiVO_4$ comprises valance and conduction bands composed of hybrid Bi 6 s/O 2p and V3d orbitals, respectively [46]. $BiVO_4$ thin films deposited from baths A and B absorb visible light in the wavelength range of < 515

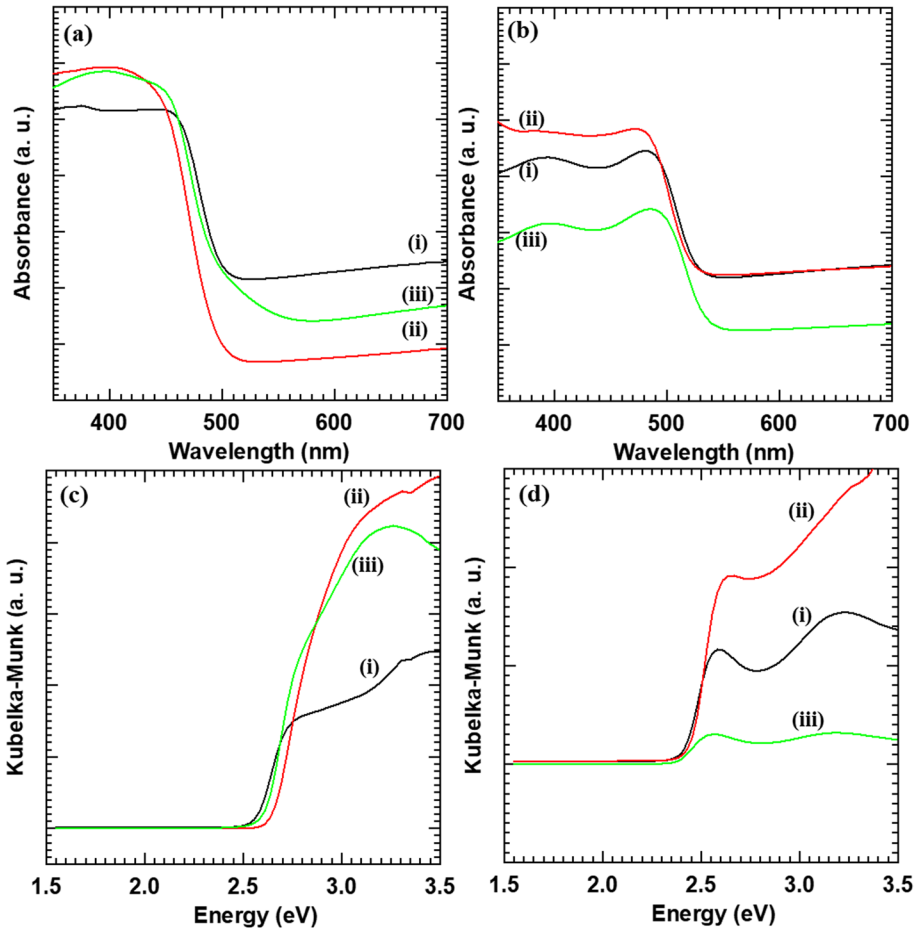

Fig. 8 UV–Vis absorbance spectra of $BiVO_4$ thin films deposited from **a** bath A [O_{Acd} (i), O_{Nut} (ii), O_{Alk} (iii)] and **b** bath B [M_{Acd} (i), M_{Nut} (ii), M_{Alk} (iii)]. Diffuse reflectance UV–Vis spectra (plotted as the Kubelka–Munk function of the reflectance, R) of $BiVO_4$ thin films deposited from **c** bath A [O_{Acd} (i), O_{Nut} (ii), O_{Alk} (iii)] and **d** bath B [M_{Acd} (i), M_{Nut} (ii), M_{Alk} (iii)]

and < 530 nm, respectively, corresponding to the bandgap energies of 2.40 and 2.33 eV. The calculated bandgap energies of $BiVO_4$ thin films deposited from baths A and B are displayed in Table S1 (ESI). The $BiVO_4$ thin films deposited from 'bath A' display a blue shift in absorption edge compared to films prepared from 'bath B', which is attributed to the smaller size of $BiVO_4$ dispersed nanoparticles deposited from 'bath A'. The lower bandgap values of $BiVO_4$ thin films deposited from 'bath B' are attributed to the growth of facet-controlled micrometer-size octahedral $BiVO_4$ crystals. This type of faceted morphology can assist the easy transport of excitons to the surface of the semiconductor, leading to effective charge separation and improved PEC activity [47].

4 Photoelectrochemical measurements

The PEC characteristics of the $BiVO_4$ photoanodes deposited on SS substrates were studied with LSV and chronoamperometry measurements. All the $BiVO_4$ photoanodes exhibited notable photocurrent in potassium phosphate buffer electrolyte, highlighting their functional PEC performance (J–V curves in Fig. S7 in ESI). The photocurrent densities at 1.23 V (vs. RHE) for all $BiVO_4$ photoanodes are summarized in Table S2 in ESI. As shown in Fig. 9a, the $BiVO_4$ thin film photoanode deposited from bath B display higher current density than the nanoparticulate $BiVO_4$ photoanode indicating its improved PEC performance. The variation in the PEC performances of $BiVO_4$ thin films deposited from baths A and B can be ascribed to their distinct morphologies.

As represented in Fig. 9b, the shape-selective $BiVO_4$ thin films display significant variation in PEC performance with bath pH. Among the shape-selective $BiVO_4$ thin films, M_{Acd} thin film exhibited the highest photocurrent density of 2.75 mA cm^{-2} at 1.23 V (vs. RHE), indicating improved PEC performance. The improved performance of M_{Acd} thin film is attributed to the well-defined compact octahedral $BiVO_4$ morphology with exposed {121} facets, which provides more surface-active facets with abundant active sites for effective PEC reactions. The water oxidation kinetics as well as charge-separation and transfer properties of $BiVO_4$ photoanodes are highly influenced by its crystal facets. From experimental findings it is concluded that, the water oxidation kinetics of $BiVO_4$ photoanode is based on the adsorption and dissociation energy of water molecules on its crystal

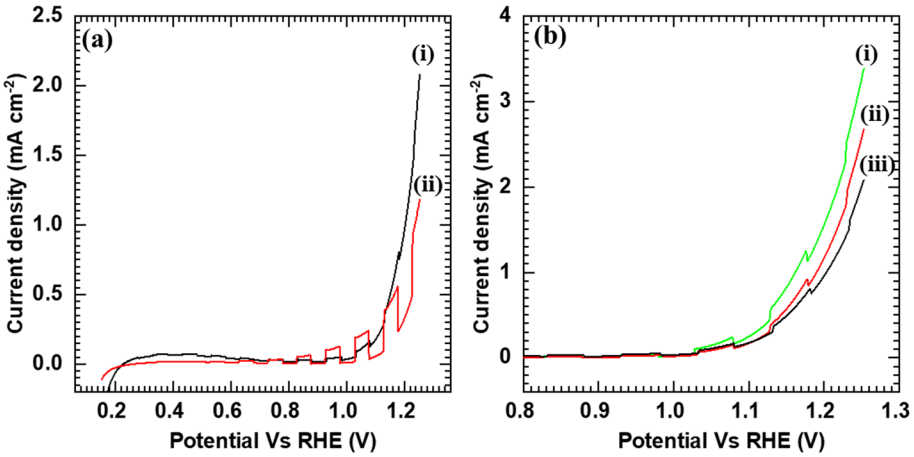

Fig. 9 **a** Chopped J–V curves of (i) faceted $BiVO_4$ and (ii) nanoparticulate $BiVO_4$ thin films. **b** Chopped J–V curves of (i) M_{Acd}, (ii) M_{Nut} and (iii) M_{Alk} $BiVO_4$ thin films

facets. Theory calculations suggested that, the adsorption of water molecules on the {121} facets of $BiVO_4$ is energetically favorable for successive dissociation and oxidation compared to the {010} and {110} low-index facets [48]. Hence, the present octahedral $BiVO_4$ photoanodes with {121} facets are highly efficient for improved PEC performance. However, the shape-selective M_{Nut} and M_{Alk} thin films display lower PEC performance than M_{Acd}, which is attributed to the decreased compactness and sharpness of $BiVO_4$ microcrystallites.

The PEC performance of $BiVO_4$ thin film photoanodes is highly dependent on their thickness. It is observed that; as the pH of deposition bath decreases, thickness of $BiVO_4$ thin film increases. The PEC performance of $BiVO_4$ thin film increases with increase in $BiVO_4$ film thickness. The plot of thickness of $BiVO_4$ thin film with pH variation is shown in Fig. S8 (ESI).

Furthermore, the photocurrent density vs. time (J–t) measurements were used to probe the long-term PEC stability of $BiVO_4$ thin film photoanodes under a constant electrical bias of 1.23 V vs. RHE and illumination. 0.1 M potassium phosphate buffer solution (pH 7) mixed with 0.2 M Na_2SO_3 hole scavenger was used as an electrolyte [49]. As shown in Fig. 10a, b, all the $BiVO_4$ thin film photoanodes deposited from baths A and B display stable photocurrent density over 60 min with a slight decrease at the initial 5 min. The $BiVO_4$ thin film photoanode deposited with alkaline bath A (O_{Alk}) exhibited stabilized photocurrent density of 0.39 mA cm^{-2}. On the other hand, $BiVO_4$ thin film photoanodes deposited from acidic bath B (M_{Acd}) display the highest stabilized photocurrent density of 2.73 mA cm^{-2}. Present results highlighting the high photostability of $BiVO_4$ thin film photoanodes against applied bias and light illumination.

In addition, the ABPE was calculated for all $BiVO_4$ thin film photoanodes from respective J–V curves obtained and plotted in Fig. 10c, d. The shape-selective $BiVO_4$ thin film photoanodes display a higher ABPE of 0.084% compared to nanoparticulate $BiVO_4$. The improved ABPE of shape-selective $BiVO_4$ thin film photoanodes is attributed to the fast charge transfer kinetics on the {121} crystal facet and quick transport of excitons in well-defined compact octahedral $BiVO_4$ crystals. Furthermore, the charge separation efficiency of $BiVO_4$ photoanodes was evaluated and displayed in Fig. 11. The shape-selective $BiVO_4$ thin film photoanodes display a maximum charge separation efficiency of 45.5% for the M_{Acd} sample.

5 Photoelectrochemical reaction mechanism

The band structure of $BiVO_4$ thin film photoanodes was mapped using CV measurements and UV–Vis spectroscopy. The scheme of the PEC reaction mechanism with band structure for $BiVO_4$ thin film photoanodes is displayed in Fig. 12. The lowest edge of the conduction band (CB) can be determined from the onset potential of the reduction peak in the CV curve (Fig. S9 in ESI) [50]. The onset potential of the reduction peak is observed at the − 0.26 V vs. Ag/AgCl corresponds to the 4.39 eV (vs. vacuum). Thus, the lowest edge of the CB is located at 4.39 eV (vs. vacuum). Judging from the bandgap energy (2.33 eV) of $BiVO_4$ thin film photoanodes, the valence band (VB) position is located at 6.72 eV (vs. vacuum) [51]. The mapped band structure of $BiVO_4$ thin film photoanodes indicates that these band positions favor the oxidation of water molecules [52].

Solar energy can be converted into chemical energy in PEC cells via a water-splitting reaction. The overall PEC water splitting can occur via the following half-cell reactions:

$$2H^+ + 2e^- \rightarrow H_2\,(g)\ \left(\text{HER}\ :\ H_2\ \text{evolution reaction}\ :\ \text{reduction}\right),$$

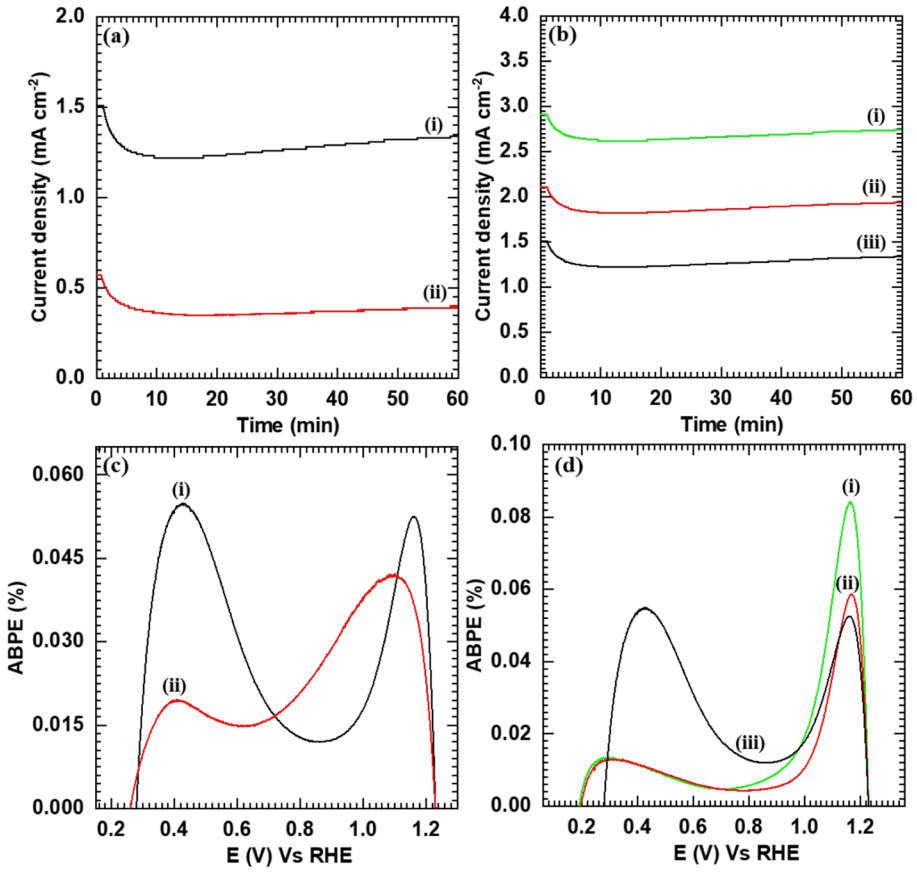

Fig. 10 **a** J–t curves of (i) faceted $BiVO_4$ and (ii) nanoparticulate $BiVO_4$ thin films. **b** J–t curves of (i) M_{Acd}, (ii) M_{Nut} and (iii) M_{Alk} $BiVO_4$ thin films. **c** ABPE curves of (i) faceted $BiVO_4$ and (ii) nanoparticulate $BiVO_4$. **d** ABPE curves of (i) M_{Acd}, (ii) M_{Nut} and (iii) M_{Alk} $BiVO_4$ thin films

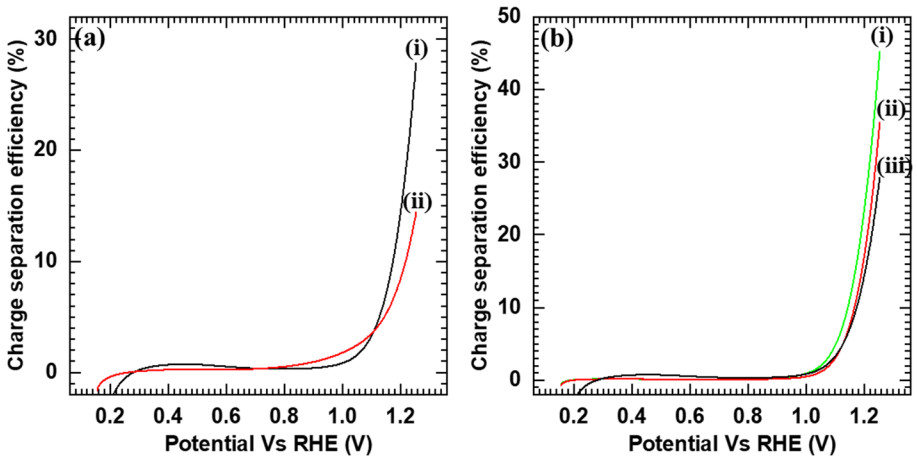

Fig. 11 **a** Charge separation efficiency curves of (i) faceted $BiVO_4$ and (ii) nanoparticulate $BiVO_4$ thin films. **b** Charge separation efficiency curves of (i) M_{Acd}, (ii) M_{Nut} and (iii) M_{Alk} $BiVO_4$ thin films

$$2H_2O + O_2(g) + 4H^+ + 4e^-$$
$$\left(\text{OER}: \ O_2\text{evolution reaction}: \ \text{oxidation}\right),$$

$$2H_2O + O_2(g) + 2H_2(g)(\text{Overall water splitting reaction}).$$

When photons having energy equal to or greater than the bandgap energy of $BiVO_4$ ($h\nu \geq E_{gBiVO_4}$) are incident on it, then electron–hole (e^-–h^+) pairs are generated. The photogenerated electrons are transferred to the CB, whereas holes are transferred to the VB of $BiVO_4$. After the charge separation, photogenerated electrons are transferred to the surface of the cathode (Pt plate), where a reduction reaction (H_2 evolution) occurs, while photogenerated holes are transferred to the surface of the anode ($BiVO_4$), where an oxidation reaction (O_2 evolution) takes place [4].

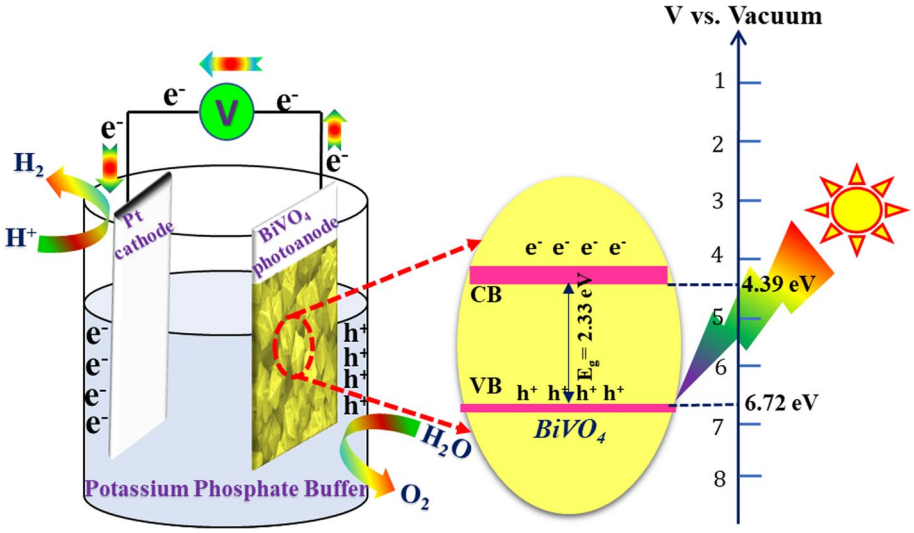

Fig. 12 Scheme of visible light induced PEC water splitting mechanism using $BiVO_4$ photoanode

6 Conclusions

The highly photoactive facet-controlled $BiVO_4$ thin film photoanodes are synthesized via a cost-effective CBD method in the present work. The anionic precursor variation leads to the tailoring of the crystal shape of $BiVO_4$ from dispersed nanoparticles to faceted microcrystals. The shape-selective faceted $BiVO_4$ photoanodes display enhanced photoactivity compared to the nanoparticulate type, which clearly underscores the effectiveness of crystal facets control in improving the PEC performance of $BiVO_4$ thin films. The $BiVO_4$ thin film photoanode deposited from an acidic bath exhibited the maximum photocurrent density (2.75 mA cm^{-2} at 1.23 V vs. RHE), good photostability and charge separation efficiency (45.5%) attributed to its well-defined compact octahedral morphology. Thus, the present results highlight the effectiveness of faceted microstructure for improved photoactivity in PEC water splitting.

Supplementary Information The online version contains supplementary material available at https://doi.org/10.1007/s00339-023-07164-1.

Acknowledgements The authors would like to thank the Science and Engineering Research Board (SERB), a statutory body of the Department of Science and Technology (DST), Government of India, for awarding the Ramanujan Fellowship (SB/S2/RJN-090/2017) and core research grant (CRG/2019/006059). The authors thank D. Y. Patil Education Society, Kasaba Bawada, Kolhapur, for financial support through research project sanction No. DYPES/DU/R&D/2022/2352.

Author contributions SPK: investigation, methodology, writing—original manuscript, YMC: validation, VVM: validation, PDS: formal analysis, SVT: software, SAP: software, UMP: data curation, KVG: writing—review and editing, DBM: resources, AUP: resources, JLG: conceptualization, supervision, funding acquisition, writing—review and editing.

Data availability The authors declare that the data supporting the findings of this study are available within this paper and its Supplementary Information files.

Declarations

Conflict of interest The authors declare that they have no known competing financial interests or personal relationships that could have appeared to influence the work reported in this paper.

References

1. R.M.N. Yerga, M.C.A. Galvan, F.D. Valle, J.A.V. Mano, J.L.G. Fierro, Chem. Sus. Chem. **2**, 471–485 (2009)
2. A.A. Ismail, D.W. Bahnemann, Sol. Energy Mater. Sol. Cells **128**, 85–101 (2014)
3. I. Paramasivam, H. Jha, N. Liu, P. Schmuki, Small **8**, 3073–3103 (2012)
4. W. Yang, R.R. Prabhakar, J. Tan, S.D. Tilley, J. Moon, Chem. Soc. Rev. **48**, 4979–5015 (2019)
5. J. Li, N. Wu, Catal. Sci. Technol. **5**, 1360–1384 (2015)
6. M. Zayed, A.M. Ahmed, M. Shaban, Int. J. Hydrog. Energy **44**, 17630–17648 (2019)
7. H. Magnan, D. Stanescu, M. Rioult, E. Fonda, A. Barbier, J. Phys. Chem. C **123**, 5240–5248 (2019)
8. S. Shen, J. Chen, L. Cai, F. Ren, L. Guo, J. Materiomics **1**, 134–145 (2015)
9. V.M. Aroutiounian, V.M. Arakelyan, G.E. Shahnazaryan, Sol. Energy **78**, 581–592 (2005)
10. S. Chandrasekaran, L. Yao, L. Deng, C. Bowen, Y. Zhang, S. Chen, Z. Lin, F. Peng, P. Zhang, Chem. Soc. Rev. **48**, 4178–4280 (2019)
11. W. Xu, W. Tian, L. Li, RRL Solar **5**, 2000412 (2021)
12. M. Suryawanshi, S.W. Shin, U. Ghorpade, D. Song, C.W. Hong, S.-S. Han, J. Heo, S.H. Kang, J.H. Kim, J. Mater. Chem. A **5**, 4695–4709 (2017)
13. M.G. Tecedor, D.C. Morcoso, R.F. Climent, S. Gimenez, Adv. Mater. Interfaces **6**, 1900299 (2019)
14. Z.F. Huang, L. Pan, J.J. Zou, X. Zhang, L. Wang, Nanoscale **6**, 14044–14063 (2014)
15. G. Xi, J. Ye, Chem. Commun. **46**, 1893–1895 (2010)

16. J. Zhu, F. Fan, R. Chen, H. An, Z. Feng, C. Li, Angew. Chem. **127**, 9239–9242 (2015)
17. G. Liu, Y. Zhu, Q. Yan, H. Wang, P. Wu, Y. Shen, Y. Doekhi-Bennani, Sci. Total. Environ. **762**, 143086 (2021)
18. S.S. Han, J.Y. Park, H.S. Hwang, H.R. Choe, K.M. Nam, E.J. Cho, Chem. Sus. Chem. **12**, 3018–3022 (2019)
19. X. Zhai, Z. Li, Z. Lu, G. Wang, P. Li, Y. Gao, X. Huang, W. Huang, H. Uji-i, G. Lu, J. Colloid, Interface Sci. **542**, 207–212 (2019)
20. Y. Zhang, H. Gong, Y. Zhang, K. Liu, H. Cao, H. Yan, J. Zhu, Eur. J. Inorg. Chem. **2017**, 2990–2997 (2017)
21. H. Li, G. Liu, X. Duan, Mater. Chem. Phys. **115**, 9–13 (2009)
22. G.S. Kamble, Y.-C. Ling, Sci. Rep. **10**, 12993 (2020)
23. I. Khan, A.Z. Khan, A. Sufyan, M.Y. Khan, S.I. Basha, A. Khan, Ultrason. Sonochem. **68**, 105233 (2020)
24. G. Zhang, Y. Meng, B. Xie, Z. Ni, H. Lu, S. Xia, Appl. Catal. B Environ. **296**, 120379 (2021)
25. D. Wang, H. Jiang, X. Zong, Q. Xu, Y. Ma, G. Li, C. Li, Chem. Eur. J. **17**, 1275–1282 (2011)
26. R.S. Mane, C.D. Lokhande, Mater. Chem. Phys. **65**, 1–31 (2000)
27. M.C. Neves, T. Trindade, Thin Solid Films **406**, 93–97 (2002)
28. L. Xia, J. Li, J. Bai, L. Li, S. Chen, B. Zhou, Nano-Micro Lett. **10**, 11–21 (2018)
29. G. Rahman, A. Akhtar, N.A. Khan, S.Y. Chae, A.U.H.A. Shah, O.-S. Joo, Optik **224**, 165516 (2020)
30. M. Han, X. Chen, T. Sun, O.K. Tan, M.S. Tse, Cryst. Eng. Comm. **13**, 6674–6679 (2011)
31. W. Luo, Z. Wang, L. Wan, Z. Li, T. Yu, Z. Zou, J. Phys. D Appl. Phys. **43**, 405402–405409 (2010)
32. T.W. Kim, Y. Ping, G.A. Galli, K.S. Choi, Nat. Commun. **6**, 1–10 (2015)
33. X. Zhong, H. He, M. Yang, G. Ke, Z. Zhao, F. Dong, B. Wang, Y. Chen, X. Shi, Y. Zhou, J. Mater. Chem. A **6**, 10456–10465 (2018)
34. S. Bera, S.A. Lee, W.-J. Lee, J.-H. Kim, C. Kim, H.G. Kim, H. Khan, S. Jana, H.W. Jang, S.-H. Kwon, A.C.S. Appl, Mater. Interfaces **13**, 14291–14301 (2021)
35. J.L. Gunjakar, A. Inamdar, B. Hou, S. Cha, S.M. Pawar, A.A.A. Talha, H.S. Chavan, J. Kim, S. Cho, S. Lee, Y. Jo, H. Kim, H. Im, Nanoscale **10**, 8953–8961 (2018)
36. J. Livage, Coord. Chem. Rev. **178–180**, 999–1018 (1998)
37. Y. Hayashi, Coord. Chem. Rev. **255**, 2270–2280 (2011)
38. W. Sun, M. Xie, L. Jing, Y. Luan, H. Fu, J. Solid State Chem. **184**, 3050–3054 (2011)
39. A.K. Adepu, V. Katta, N. Venkatathri, New J. Chem. **41**, 2498–2504 (2017)
40. T.D. Nguyen, V.H. Nguyen, S. Nanda, D.N. Vo, V.H. Nguyen, T.V. Tran, L.X. Nong, T.T. Nguyen, L.G. Bach, B. Abdullah, S.S. Hong, T.V. Nguyen, Environ. Chem. Lett. **18**, 1779–1801 (2020)
41. T.D. Nguyen, Q.T.P. Bui, T.B. Le, T.M. Altahtamouni, K.B. Vu, D.V.N. Vo, N.T.H. Le, T.D. Luu, S.S. Hong, K.T. Lim, RSC Adv. **9**, 23526–23534 (2019)
42. T.S. Dabodiya, P. Selvarasu, A.V. Murugan, Inorg. Chem. **58**, 5096–5110 (2019)
43. A. Helal, S.M. El-Sheikh, J. Yu, A.I. Eid, S.A. El-Haka, S.E. Samra, J. Nanopart. Res. **22**, 132 (2020)
44. Z. Jiang, Y. Liu, T. Jing, B. Huang, X. Zhang, X. Qin, Y. Dai, M.-H. Whangbo, J. Phys. Chem. C **120**, 2058–2063 (2016)
45. Y. Deng, L. Tang, G. Zeng, C. Feng, H. Dong, J. Wang, H. Feng, Y. Liu, Y. Zhou, Y. Pang, Environ. Sci. Nano **4**, 1494–1511 (2017)
46. K.K. Dey, S. Gahlawat, P.P. Ingole, J. Mater. Chem. A **7**, 21207–21221 (2019)
47. R.A. Rather, A. Mehta, Y. Lu, M. Valant, M. Fang, W. Liu, Int. J. Hydro. Eng. **46**, 21866–21888 (2021)
48. M. Yang, H. He, A. Liao, J. Huang, Y. Tang, J. Wang, G. Ke, F. Dong, L. Yang, L. Bian, Y. Zhou, Inorg. Chem. **57**, 15280–15288 (2018)
49. X. Zhang, B. Zhang, K. Cao, J. Brillet, J. Chen, M. Wang, Y. Shen, J. Mater. Chem. A **3**, 21630–21636 (2015)
50. J.L. Gunjakar, T.W. Kim, H.N. Kim, I.Y. Kim, S.J. Hwang, J. Am. Chem. Soc. **133**, 14998–15007 (2011)
51. K. Saruwatari, H. Sato, T. Idei, J. Kameda, A. Yamagishi, A. Takagaki, K. Domen, J. Phys. Chem. B **109**, 12410–12416 (2005)
52. H. Shi, H. Guo, S. Wang, G. Zhang, Y. Hu, W. Jiang, G. Liu, Energy Fuels **36**, 11404–11427 (2022)